

Significant reduction of surface solar irradiance induced by aerosols in a suburban region in northeastern China

Xiangao Xia¹, Hongbin Chen¹, Zhanqing Li^{1,2}, Pucai Wang¹, Jiankai Wang¹

1. Institute of Atmospheric Physics, Chinese Academy of Sciences, Beijing, China,
100021

2. Department of Atmospheric and Oceanic Science, University of Maryland,
Maryland, U.S.A.

Submitted to
Journal of Geophysical Research – Atmosphere
A special issue on
East-Asian Study of Tropospheric Aerosols: an International Regional Experiment
(EAST-AIRE)

Abstract

In the spring of 2005, a sunphotometer and a set of broadband pyranometers were installed in Liaozhong, a suburban region in northeastern China. Aerosol properties derived from sunphotometer measurements and aerosol-induced changes in downwelling shortwave surface irradiances are analyzed in this paper. It is shown that the mean aerosol optical depth (AOD) at 500 nm is 0.63. The day-to-day variation of aerosol optical depth is dramatic, with a maximum daily AOD close to 2.0 and a minimum value close to the background level. Dust activities generally produce heavy aerosol loading characterized by larger particle sizes and less absorption than those observed under normal conditions. The reduction of instantaneous direct shortwave surface irradiance per unit of AOD is 404.5 Wm^{-2} . About 63.8% of this reduction is offset by an increase in diffuse irradiance, consequently, one unit increase in AOD leads to a decrease in global surface irradiance of 146.3 Wm^{-2} . The diurnal aerosol direct radiative forcing efficiency is about -47.4 Wm^{-2} . Overall, aerosols reduce about 30 Wm^{-2} per day of surface net shortwave irradiance in this suburban region.

1. Introduction

Much attention has been paid to the connection between the greenhouse effect brought on by human activities and global climate change. Human activities also result in the emission of large amounts of aerosols, an important atmospheric constituent that can influence global climate [Schwartz and Buseck, 2000]. Aerosols directly influence the Earth's radiative balance through the backscattering and absorption of shortwave (solar) radiation and indirectly by influencing cloud properties and lifetimes [Charlson *et al.*, 1992]. Atmospheric aerosol loadings have undoubtedly increased since the Industrial Revolution. This in turn has likely caused cooling of the climate system. Calculations suggest that inclusion of aerosols as an important forcing agent can improve the simulation of climate change [IPCC, 2001].

The global annually averaged direct radiative forcing at the top of the atmosphere by aerosols is estimated to be in the range of -0.5 to 0.2 Wm^{-2} [Haywood and Boucher, 2000]. Because of the relatively short lifetime of aerosol particles and their large regional variability, instances of strong localized direct forcing can occur. On a regional scale, it is suggested that aerosols are already affecting surface forcing, atmospheric heating, and precipitation [Ramanathan *et al.*, 2001]. Another important effect is that aerosols substantially decrease downward shortwave irradiances at the surface, which then impacts crop growth and solar energy availability [Li, 1998; Chameides *et al.*, 1999; Satheesh and Ramanathan, 2000]. There is no doubt of the importance of aerosols with regard to climate and the environment system. However, large uncertainties in the chemical, physical, and radiative properties of atmospheric aerosols render the quantitative assessment of aerosol effects on climate and environment problematic.

For example, rapid economic growth and population expansion over the last twenty years has led to a significant increase in aerosol optical depth (AOD) over much of China. The average AOD at 750 nm observed at 46 stations in China increased from 0.38 in 1960 to 0.47 in 1990 [Luo *et al.*, 2001]. High aerosol loading

over much of China is evident from satellite and ground-based measurements [Li *et al.*, 2003; Xia *et al.*, 2005; Xin *et al.*, 2006]. A case study showed that dust cloud crossed the Pacific Ocean within 5 day and impacted severely the optical and the concentration environment of the downwind region [Husar *et al.*, 2001]. An extremely wide range of aerosol loading, size and absorption are derived from multiyear ground-based network observations in East Asia region [Eck *et al.*, 2005]. The increase in aerosol loading partly accounts for a notable decrease of sunshine duration and downward surface solar irradiance [Liang, 2005]. Heavy aerosol loading and strong aerosol absorption were suggested as reasons for the regional temperature changes seen in the Sichuan Basin and precipitation pattern changes from the mid-1970's to the present [Li *et al.*, 1995; Xu, 2001; Menon *et al.*, 2002]. Aerosols can impact crop production through their effect on surface irradiance availability for crop photosynthesis [Chameides *et al.*, 1999]. It should be noted that these studies are based upon some hypotheses due to a lack of actual observations and a number of issues remain open. In-situ observations made in the continental source region on a continual basis are urgently required in order to portray the spatial and temporal variations of the complex aerosols located throughout the vast territory of China and their effects on climate and environment [Li, 2004]. This is the goal of the East Asian Study of Tropospheric Aerosols: an International Regional Experiment (EAST-AIRE) [Li *et al.*, 2006]

In April 2005, a comprehensive observation site was established in a suburban region in northeast China as a part of EAST-AIRE, in support of an air-borne campaign measuring the profiles of atmospheric aerosols and gases conducted in the region [Dickerson *et al.* 2006, manuscript in preparation for the same special issue]. A CIMEL sun/sky radiometer and a set of broadband solar radiometers were installed side by side. The measured aerosol properties and their effect on surface insolation are discussed in this paper.

The paper is organized as follows. The experimental site and the data collected are described in the following section. Section 3 introduces the methodology. Section 4 presents the analysis of aerosol properties derived from the sunphotometer and

aerosol direct forcing is given in section 5. The conclusion and discussions are presented in the last section.

2. Site Description and Instrumentation

In April 2005, a radiation station was established in Liaozhong County (41° 30' N, 120° 42' E, 15 m ASL), a suburban region in northeast China. The site is located about 70 km southeast of Shenyang, the major city in northeast China (650 km to Beijing) with a population of approximately 4 million. The site is located along one of the pathways taken by dust storms that occasionally blow across the East Asian continent [Sun *et al.*, 2001]. The atmosphere above the site in spring is characterized by frequent haziness, mainly due to anthropogenic pollution and occasional outbreaks of mineral dust. A CIMEL sun/sky radiometer and a set of broadband radiometers were installed side by side. In addition, a Total Sky Imager (TSI) was employed to take snapshots of the overhead sky condition every minute during daytime hours. The instruments were installed on the roof (more than 6 meters above ground) of a two-level building where the field of view is unobstructed in all directions.

2.1. Aerosol Robotic Network (AERONET) Data

A detailed description of the CIMEL sun/sky radiometer and its products is presented by Holben *et al.* [1998]. The radiometer takes measurements of AOD at seven wavelengths (340, 380, 440, 500, 670, 870 and 1020 nm). The uncertainty in AOD is 0.01~0.02 [Eck *et al.*, 1999]. The measurements at 940 nm are used for the derivation of the water vapor column amount. Aerosol size distribution, refractive index and single-scattering albedo are retrieved from the sky radiance measurements and AODs [Dubovik *et al.*, 2000]. The AERONET data we use here is the level 2.0 quality-assured and cloud-screened dataset (available from the AERONET website, <http://aeronet.gsfc.nasa.gov/T>). The data have been pre- and post-field calibrated, automatically cloud screened [Smirnov *et al.*, 2000] and manually inspected. Note that a spheroid particle shape assumption, rather than a spherical particle shape

assumption, is used to simulate aerosol scattering during dust periods. This minimizes the non-spherical effects of dust on the retrievals, such as the artificial spectral dependence of the real part of the refractive index and the artificially high concentrations of small particles (radius $<0.1 \mu\text{m}$) [Dubovik et al., 2002a].

2.2. Broadband Solar Radiation Data

Global, direct and diffuse solar radiation was measured by a set of state-of-the-art broadband pyranometers (see Table 1). Solar radiation is sampled every second but the 1-minute mean is saved to the data logger. The Eppley Normal Incidence Pyrheliometer (NIP) and black&white radiometer (B&W) were installed on a solar tracker to measure solar direct and diffuse radiation, respectively. The pyranometers were factory-calibrated immediately before the installation. The thermal offset of the pyranometers during the daytime is corrected through adding the absolute mean observation at night before and after the daytime. The data are quality checked using the Baseline Surface Radiation Network (BSRN) quality control procedure [Ohmura et al., 1998]. More importantly, we used a redundant set of broadband pyranometers in order to ensure the accuracy of the global solar irradiance measurements and to rule out possible biases due to any offset in the calibration coefficients of a single instrument. This inter-comparison of global irradiances measured by the two pyranometers and the global irradiances calculated as the sum of the NIP (multiplied by cosine of solar zenith angle) and B&W measurements helps detect any data anomaly, identify its causes and correct the problem. Although the instruments were manufactured by two different companies and have different sensitivities, their disagreements remained persistently low ($<10 \text{ Wm}^{-2}$) except for very few occasional jumps due to drifts in horizontal leveling.

2.3. Total Sky Imager (TSI) data

To help separate cloudy and hazy conditions, a total sky imager (TSI-440) was set up at the site, which takes snapshots of the sky on a continuous 1-minute basis during each day from sunrise to sunset. The TSI-440 model is a full color sky camera with a

software package that operates the instrument and performs some data processing functions. It captures images in JPEG format data files, which can be analyzed for fractional cloud cover. From the high-frequency snapshot images, a movie of the sky conditions is generated for each day. It has proven to be a very useful tool to assist in the separation of cloudy scenes from hazy clear-sky scenes, as clouds are generally more variable than the atmospheric aerosols.

3. Methodology

The goal of this research was to study aerosol effects on solar radiation at the surface under clear conditions, so the first task was to obtain aerosol and radiation data for cloudiness periods. This is achieved by an empirical clear-sky detection method that is based on 1-minute radiation data. The method was introduced as follows.

It is shown that global shortwave radiation under clear sky can be simulated by a power law function of the cosine of solar zenith angle [*Long and Ackerman, 2000*].

$$F_{global} = a \times \cos(\theta)^b \quad (1)$$

where a indicates the expected global radiation when θ is equal to zero and b determines variation of global radiation with θ . The value of b is close to 1.2 [*Long and Ackerman, 2000*], so coefficient b is set 1.2 and only coefficient a is allowed to increase gradually to simulate possible global radiation for clear sky with different aerosol loading. The process is terminated and corresponding coefficient a is saved if 80% of observations are less than the computed values by equation 1 with the specified coefficients. An observation is considered to be influenced by cloud if the absolute relative deviation of observation from the corresponding computed values is greater than 20% (the first check). Next, the observations are normalized by the simulated values. The variability of the normalized irradiances is tested by computing a running standard deviation over a 30-minute period. The observation is deemed

affected by cloud if the standard deviation is greater than 0.02 (the second check). The parameters used in the clear-sky detection method were tuned by a trial and error method based on sky condition as seen more clearly from TSI animation. Figure 1 showed an example illustrating how the algorithm discriminates clear-sky observations.

The filtered clear-sky radiation observations are then collocated with CIMEL sunphotometer data. The measured downward shortwave irradiances are first compared with simulations by a radiative transfer model. The model is also used to compute the background-level solar radiation using the water vapor column amount (from CIMEL retrievals), the ozone column amount (from the Total Ozone Mapping Spectrometer, TOMS) and MODIS surface albedo as model inputs. The aerosol effect on instantaneous global, direct, and diffuse surface irradiances is computed as the difference between observations and the corresponding model simulations of the background conditions. Note that the aerosol effect presented here includes contributions from both anthropogenic and background aerosols. The diurnal mean aerosol direct radiative forcing (ADRF) can better represent the climatic effects of aerosol, but calculating a diurnal mean is not straightforward because cloudy-sky periods frequently intervene clear-sky periods. Therefore, a method is required to interpolate the clear-sky measurements when there were no observations available. The method of *Conant* [2000] is used to derive diurnal values from instantaneous measurements. On a day-to-day basis, a diurnal cycle of shortwave irradiances is simulated by a radiative transfer model using AOD and the water vapor column amount as its inputs. The ratio of measurements of instantaneous shortwave irradiance to the model simulation is computed. The ratio is then multiplied by the model diurnal cycle to convert the instantaneous measurements to corresponding diurnal cycles. The derived curve is lastly integrated over 24 hours to obtain a diurnal mean irradiance.

4. Results

The analysis of aerosol properties derived from sunphotometer measurements is presented firstly in this section. The measurements of solar irradiance are compared

against simulations of radiative transfer model that is driven by sunphotometer data. Aerosol instantaneous and diurnal mean radiative forcing is derived by the collocated AOD and radiation data.

4.1. Aerosol Properties from Sunphotometer Data

The daily mean AOD at 500 nm (hereafter AOD means aerosol optical depth at 500 nm if not specified) is presented in Figure 2a. Large variations in the AOD are noted, with AOD ranging from a minimum of ~ 0.11 (26 May) to a maximum of 1.95 (17 April). The mean AOD value from April to June in Liaozhong is 0.63 (the standard deviation is 0.46), which is roughly a factor of 6 larger than values reported for background continental air masses ($\sim 0.1-0.15$) [Halothore *et al.*, 1992; Bergin *et al.*, 2000]. The mean AOD in Liaozhong is similar to the mean AOD measured in heavily polluted air masses in a valley site (0.68) [Yu *et al.*, 2000] and off the east coast of the United States (0.56) [Reddy *et al.*, 1990]. The mean AOD in Liaozhong is also within the range of the values reported in other suburban regions of China, such as 0.61 in Linan [Xu *et al.*, 2002], 0.56 in Miyun and 0.60 in Xinfeng [Zhang *et al.*, 2002], 0.77 in Xianghe [Li *et al.*, 2006]. The outstanding feature in Liaozhong is that the AOD varies dramatically, with the standard deviation a factor of 2-4 higher than that in other regions.

The Angstrom wavelength exponent (α) provides an indication of the aerosol particle size. The α of dust particles are on the order of 0.1-0.6 [Seinfeld and Pandis, 1998]; however, most fine mode particles are anthropogenic in origin and generally have α larger than 1.5. The mean α , which is computed from a linear regression of aerosol optical depth versus wavelength at a logarithmic scale with data from 440, 500, 670, and 870 nm, is 0.96 ± 0.34 , which is close to observations in Japan [Eck *et al.*, 2005]. The mean α increases from 0.74 (± 0.40) in April to 1.08 (± 0.29) in May and 1.03 (± 0.18) in June. As seen in Figure 2b, α shows remarkable temporal variability. The months of April and May showed a few days with α less than 0.3. This is indicative of the large input of coarse mode dust aerosols to the atmosphere. The time series of the fine mode contribution to aerosol optical depth is shown in Figure 3a. Fine mode particles account for less than 30% of the extinction at 670 nm when α

is less than 0.3. The mean value is about 0.73 for α larger than 0.75, which is close to that in downwind regions, such as in Korea and Japan [Eck *et al.*, 2005].

The mean single scattering albedo (ω) is ~ 0.90 . The value is somewhat less than ω in suburban regions such as in Paris and Maryland, but it is closer to ω in other urban regions, such as in Beijing and Kanpur [Dubovik *et al.*, 2002b; Eck *et al.*, 2005; Xia *et al.*, 2006] and in Xianghe (a remote suburb of Beijing) [Li *et al.* 2006]. Note that ω shows a large temporal variability (Figure 3b). Dust particles generally have larger ω that increase with wavelength; however, ω for predominately fine mode aerosol particles have smaller ω that decrease with wavelength. This implies that dust aerosols have less absorption than anthropogenic aerosols.

4.2. Comparison of Modeled and Measured Downward Shortwave Irradiances

The Second Simulation of Satellite Signal in the Solar Spectrum (6S) is used to estimate the downward shortwave irradiances (DSWI) at the surface. The 6S model has a spectral resolution of 2.5 nm and uses the successive order of scattering algorithm to calculate the solar radiative transfer within the atmosphere [Vermote *et al.*, 1997]. The mid-latitude winter standard atmosphere is used to describe vertical profiles in the atmosphere (i.e. water vapor, temperature, pressure, ozone density profiles). The column-integrated ozone and water vapor amounts in the standard atmosphere were scaled by the ozone content data from TOMS and water vapor content data from the CIMEL sunphotometer. The aerosol inputs to the radiation transfer model are aerosol size distribution and refractive index. Aerosol size distribution parameters are fit as functions of AOD using AERONET data [Remer and Kaufman, 1998]. Note that the correlations between aerosol size parameters and AOD are derived for dust ($\alpha \leq 0.6$ and TOMS Aerosol Index (AI) > 0.6) and non-dust cases ($\alpha > 0.6$ or TOMS AI ≤ 0.6). The mean refractive index for two cases is computed and used in the simulations. The spectral optical properties (extinction, phase function and single-scattering albedo) are computed using a Mie algorithm. MODIS broadband albedo data are used to specify the surface albedo in the computation.

The calculated DSWI at the surface was first compared with pyranometer

measurements. Figure 4 shows comparisons between the calculated and the measured global irradiances from the CM21 pyranometer (a) and from the sum of direct and diffuse components (b), direct irradiances (c) and diffuse irradiances (d). The modeled means and one standard deviations of global, direct and diffuse DSWI are 663 ± 259 , 493 ± 257 , $170 \pm 91 \text{ Wm}^{-2}$, respectively. In comparison, the corresponding observation values are 652 ± 250 , 485 ± 253 , 164 ± 95 , respectively. The correlation coefficients are larger than 0.99 for global and direct irradiances. The computed and measured DSWI are in good agreement. The mean bias error ($mbe = \sum (measurements - simulations)$) between the modeled and measured global DSWI is close to 12 Wm^{-2} . As for the direct and diffuse DSWI, the mbe is 8 Wm^{-2} and 6 Wm^{-2} , respectively. The good agreement is well within the estimated absolute accuracy of the pyranometer measurements and model simulations.

4.3. Instantaneous Aerosol Effect on Surface Irradiances

Figure 5 shows instantaneous measurements of direct and diffuse irradiances and the corresponding model simulations of the background level. An important feature is that the magnitude of the irradiances varies considerably. For a fixed solar zenith angle, the aerosol-induced differences in direct irradiances between measurements and model simulations can reach more than 700 Wm^{-2} on occasion. On the contrary, diffuse irradiances dramatically increase due to aerosol scattering. In Figure 6, the difference between observed global, direct and diffuse DSWI and the corresponding model simulations of the background level are shown as the functions of the instantaneous AOD. In order to discriminate the effects of the solar zenith angle, the analysis is carried out separately for six solar zenith angle ranges. An important feature is that the DSWI generally shows a linear dependence on AOD when it is relatively low. If all data points are considered, a nonlinear equation, such as an exponential equation or a polynomial fit [Jayaraman *et al.*, 1998], is more suitable.

Table 2 presents the estimated slopes of the linear fits when $AOD < 0.8$, i.e. the change in DSWI per unit of AOD. Over the extent of solar zenith angles, the slope of

the linear fit to the direct DSWI data ranges from -217 to -522 Wm^{-2} while the slope of the linear fit to the diffuse DSWI data ranges from 116 to 349 Wm^{-2} . As a result, the global DSWI ranges from -101 to -173 Wm^{-2} . Note that a moderate scatter of data points around the fitted curves is expected. Potential reasons for the scatter include measurement uncertainties, differences in aerosol properties and the minor influence of the solar zenith angle.

4.4 Diurnal Mean ADRF at the Surface

The instantaneous irradiance changes depend on the solar zenith angle, so we computed diurnal mean irradiance changes using instantaneous measurements and 6S model simulations to focus on the AOD dependence and show what the aerosol effects would be if a given AOD persisted for the full sunlit period of a day. Figure 7 presents the diurnal mean ADRF as a function of AOD. The magnitude of the observed negative diurnal ADRF at the surface varies from about 18 Wm^{-2} to more than 90 Wm^{-2} . Performing linear regression for data with $\text{AOD} < 0.5$, the diurnal ADRF efficiency is -47.4 Wm^{-2} and -48.6 Wm^{-2} for NIP+B&W and CM21, respectively. It should be noted that daily ADRF efficiency showed a large day-to-day variation due to strong dependence of ADRF efficiency on AOD that showed dramatic daily variation. Furthermore, ADRF efficiency showed a little difference as a result of the quite differences in aerosol optical properties including spectral dependence of AOD, aerosol absorption and aerosol preferred scattering direction (aerosol asymmetry factor). For example, AOD of 1.69 at May 4 led to ADRF of 88.2 Wm^{-2} , however, AOD of 1.73 at May 15 led to ADRF of 73.2 Wm^{-2} . The rationale behind the fact is that aerosol single scattering albedo for the former (0.92) is a little less than that for the latter (0.95).

5. Conclusions

Solar broadband and spectral radiation measurements were made with four pyranometers and a sunphotometer from April to July 2005 in Liaozhong, a suburban region in northeast China. Simultaneous measurements of aerosol optical depth and

broadband radiation under clear-sky conditions were collected and aerosol-induced instantaneous and diurnal direct radiative forcing at the surface was estimated.

Aerosol loading shows a remarkable day-to-day variation, with the highest daily AOD close to 2.0 and the minimum AOD close to the background level (0.11). Aerosol loading, particle size and absorption are all seriously impacted by dust activities. The daily AOD is close to 2.0 on April 17, a day with much dust in the air, and the coarse mode aerosols contribute to more than 70% of the AOD in the visible. The single scattering albedo for the dust cases increases with wavelength while the reverse is true for non-dust cases.

Aerosols can induce significant changes in surface global shortwave irradiance and its diffuse and direct components. The reduction of instantaneous direct irradiance per unit of AOD varies from -217 Wm^{-2} to -522 Wm^{-2} , depending on the solar zenith angle. About 53% to 66% of this reduction is offset by an increase in diffuse irradiance and as a result, one unit of AOD increase results in a loss of about 101 to 173 Wm^{-2} in surface global irradiance.

The observed diurnal mean ADRF at the surface varies from about -18 Wm^{-2} to more than -90 Wm^{-2} . The ADRF efficiency computed for data with $\text{AOD} < 0.5$ is about -47 Wm^{-2} . Given that the mean AOD is 0.63, the seasonal mean reduction in surface net shortwave irradiance is about 30 Wm^{-2} in this suburban region.

Acknowledgement: The research was partly supported by the National Science Foundation of China (40250120071; 40305002) and the NASA Radiation Science Program (NNG04GE79G).

References

- Bergin, M. H., S. E. Schwartz, R. N. Halthore, J. A. Ogren, and D. L. Hlavka, Comparison of aerosol optical depth inferred from surface measurements with that determined by Sun photometry for cloud-free conditions at a continental U.S. site, *J. Geophys. Res.*, 105, 6807– 6816, 2000.
- Chameides W.L. , et al. (1999), Case study of the effects of atmospheric aerosols and regional haze on agriculture: An opportunity to enhance crop yields in China through emission controls? *PNAS*, 96, 13.626-13.633.
- Charlson, R.J, S.E. Schwartz, J.M. Hales, D. Cess, J.A. Coakley, J.E. Hansen (1992), Climate forcing by anthropogenic aerosols. *Science*, 255, 423 - 430.
- Conant, W. C. (2000), An observational approach for determining aerosol surface radiative forcing: Results from the first field phase of INDOEX, *J. Geophys. Res.*, 105, 15,347–15,360.
- Dubovik, O., A. Smirnov, B.N. Holben, M.D. King, Y.J. Kaufman et al. (2000), Accuracy assessments of aerosol optical properties retrieved from AERONET sun and sky radiance measurements. *J. Geophys. Res.* 105, 9791–9806.
- Dubovik, O., B.N. Holben, T. Lapyonok, A. Sinyuk, M.I. Mishchenko et al. (2002a), Non-spherical aerosol retrieval method employing light scattering by spheroids. *Geophys. Res. Lett.* 29(10), doi:10.1029/2001GL014506.
- Dubovik, O., B. Holben, T. F. Eck, A. Smirnov, Y. J. Kaufman, M. D. King, D. Tanre', and I. Slutsker (2002b), Variability of absorption and optical properties of key aerosol types observed in worldwide locations, *J. Atmos. Sci.*, 59, 590–608.
- Eck, T. F., B. N. Holben, J. S. Reid, O. Dubovik, A. Smirnov, N. T. O'Neill, I. Slutsker, and S. Kinne (1999), Wavelength dependence of the optical depth of biomass burning, urban and desert dust aerosols, *J. Geophys. Res.*, 104, 31,333–31,350.
- Eck, T. F., et al. (2005), Columnar aerosol optical properties at AERONET sites in central eastern Asia and aerosol transport to the tropical mid-Pacific, *J. Geophys. Res.*, 110, D06202, doi:10.1029/2004JD005274.

- Halothore, R. N., B. L. Markham, R. A. Ferrare, and T. O. Aro, Aerosol optical properties over the midcontinental United States, *J. Geophys. Res.*, 97, 18,769–18,778, 1992.
- Haywood J. and O. Boucher (2000), Estimates of the direct and indirect radiative forcing due to tropospheric aerosols: a review, *Rev. Geophys.*, 38, 513-543.
- Holben, B.N., T.E. Eck, I. Slutsker, D. Tanre, J.P. Buis, et al. (1998), AERONET—a federated instrument network and data archive for aerosol characterization. *Remote Sens. Environ.* 66, 1–16.
- Husar, R. B., et al. (2001), Asian dust events of April 1998, *J. Geophys. Res.*, 106, 18,317–18,330.
- Intergovernmental Panel on Climate Change (IPCC) (2001), Climate Change 2001: The Scientific Basis: Contribution of Working Group I to the Third Assessment Report of the Intergovernmental Panel on Climate Change, edited by J. T. Houghton et al., Cambridge Univ.Press, New York.
- Jayaraman, A., D. Lubin, S. Ramachandran, V. Ramanathan, E. Woodbridge, W. D. Collins, and K. S. Zalpuri, (1998), Direct observations of aerosol radiative forcing over the tropical Indian Ocean during the January–February 1996 pre-INDOEX cruise. *J. Geophys. Res.*, 103, 13 827–13 836.
- Li, X.W., X.J. Zhou, W.L Li, (1995), The cooling of Sichuan province in recent 40 years and its probable mechanism, *Acta. Meteo. Sinica*, 9, 57-68.
- Li C.C., et al., (2003), Characteristics of distribution and seasonal variation of aerosol optical depth in eastern China with MODIS products, *Chinese Sci. Bull.*, 48, 2488-2495.
- Li, Z., 2004, Aerosol and climate: A perspective from East Asia, in "Observation, Theory, and Modeling of the Atmospheric Variability", p501-525, World Scientific Pub. Co.
- Li, Z., 1998, Influence of absorbing aerosols on the inference of solar surface radiation budget and cloud absorption, *J. Climate*, 11, 5-17.
- Li, Z., et al., Remote sensing of aerosol optical properties and its radiative effects in Northern China, submitted to *J. Geophys. Res.*, 2006.

- Liang F. and Xia X. (2005), Long-term trends in solar radiation and the associated climatic factors over China for 1961-2000, *Annales Geophys*, 23, 2425-2432.
- Long C.N., and T.P. Ackerman, Identification of clear skies from broadband pyranometer measurements and calculation of downwelling shortwave cloud effects, *J. Geophys. Res.*, 2000, 105, 15609-15626.
- Luo, Y.F., D.R., Lu, X.J. Zhou, W.L. Li and Q. He (2001), Characteristics of the spatial distribution and yearly variation of aerosol optical depth over China in last 30 years, *J. Geophys. Res.* 106, D13, 14501-14513.
- Menon, S., J.E. Hansen, L. Nazarenko and Y.F. Luo (2002), Climate effects of black carbon aerosols in China and India. *Science* 297, 2249–2252.
- Ohmura, A., et al. (1998), Baseline Surface Radiation Network (BSRN/WCRP): New Precision Radiometry for Climate Research. *Bull. Am. Meteorol. Soc.*, 79, 2115–2136.
- Ramanathan, V., P.J. Crutzen, J.T. Kiehl and D. Rosenfeld (2001), Aerosols, climate, and the hydrological cycle. *Science*, 294, 2119–2124.
- Reddy, P. J., F. W. Kreiner, J. J. DeLuisi, and Y. Kim, Aerosol optical depth over the Atlantic derived from shipboard Sunphotometer observations during the 1988 global change expedition, *Global Biogeochem. Cycles*, 4, 225– 240, 1990.
- Remer, L.A., and Y.J. Kaufman, (1998), Dynamic aerosol model: Urban/industrial aerosol. *J. Geophys. Res.*, 103, 13 859–13 871.
- Satheesh, S. K., and V. Ramanathan (2000), Large differences in tropical aerosol forcing at the top of the atmosphere and Earth's surface. *Nature*, 405, 60– 63.
- Schwartz S.E. and P. R. Buseck (2000), Absorbing phenomena. *Science*, 288, 989-990.
- Seinfeld, J.H., S.N. Pandis (1998), Atmospheric Chemistry and Physics. Wiley-Interscience, New-York, 1326 pp.
- Smirnov, A., B.N. Holben, T.F. Eck, O. Dubovik and I. Slutsker (2000), Cloud screening and quality control algorithms for the AERONET database. *Remote Sens. Environ.* 73, 337–349.

- Sun, J., Zhang, M., Liu, T., (2001), Spatial and temporal characteristics of dust storms in China and its surrounding regions, 1960-1999: Relations to source area and climate. *J. Geophys. Res.*, 106, 10325-10333.
- Vermote E.F., D. Tanre, J.L. Deuze, M. Herman and J.J. Morcrette (1997), Second simulation of the satellite signal in the solar spectrum, 6S: an overview, *IEEE Trans. Geo. Rem. Sen.*, 35, 675-686.
- Xia, X. A., H. B. Chen, P. C. Wang, X. M. Zong, and P. Goulob (2005), Aerosol properties and their spatial and temporal variations over north China in spring 2001, *Tellus, Ser. B*, 57, 28–39.
- Xia, X. A., H. B. Chen, P. C. Wang, W. X. Zhang, P. Goloub, B. Chatenet, T. F. Eck, and B. N. Holben (2006), Variation of column-integrated aerosol properties in a Chinese urban region, *J. Geophys. Res.*, 111, D05204, doi:10.1029/2005JD006203.
- Xin, J., Y. Wang, Z. Li, P. Wang, W.-M. Hao, B.L. Nordgren, G. Liu, S. Hubo, The aerosol optical depth and Angstrom exponent of typical aerosols observed in the Chinese Sun Hazemeter Network from August 2004 to September 2005, *submitted*.
- Xu, J., M. H. Bergin, R. Greenwald, and P. B. Russell, Direct aerosol radiative forcing in the Yangtze delta region of China: Observation and model estimation, *J. Geophys. Res.*, 108(D2), 4060, doi:10.1029/2002JD002550, 2003.
- Yu, S., V. K. Saxena, B. N. Wenny, J. J. Deluisi, G. K. Yue, and I. V. Petropavlovskikh, A study of the aerosol radiative properties needed to compute direct aerosol forcing in the southeastern US, *J. Geophys. Res.*, 105, 24,739–24,749, 2000.
- Zhang J.H., Mao J.T. Wang M.H., Analysis of aerosol extinction characteristics in different area of China, *Advan. Atmos. Sci.*, 2002, 19, 136-152.

Table 1. The broadband pyranometers installed in Liaozhong during spring 2005.

	Global	Direct	Diffuse
Instrument	CM21/CM11	NIP	black&white
Wavelength (nm)	305-2800	285-2800	285-2800
Manufacturer	Kipp-Zonen	Eppley	Eppley

Table 2. The linear fits of downwelling shortwave irradiance differences (measurements minus model simulations of the background level) to aerosol optical depth at 500 nm for six solar zenith angle ranges. The slope is computed for data points with aerosol optical depth less than 0.8.

Solar zenith angle		20-30°	30-40°	40-50°	50-60°	60-70°	70-80°	mean
Global	Slope	-154.3	-173.1	-158.2	-167.7	-123.4	-101.0	-146.3
	r ²	0.93	0.90	0.87	0.94	0.87	0.91	
Direct	Slope	-473.7	-522.5	-466.6	-442.7	-304.1	-217.0	-404.5
	r ²	0.96	0.93	0.90	0.94	0.85	0.83	
Diffuse	Slope	319.5	349.5	308.4	274.9	180.7	116.0	258.2
	r ²	0.94	0.93	0.88	0.90	0.77	0.71	
Data points		116	113	72	61	80	66	

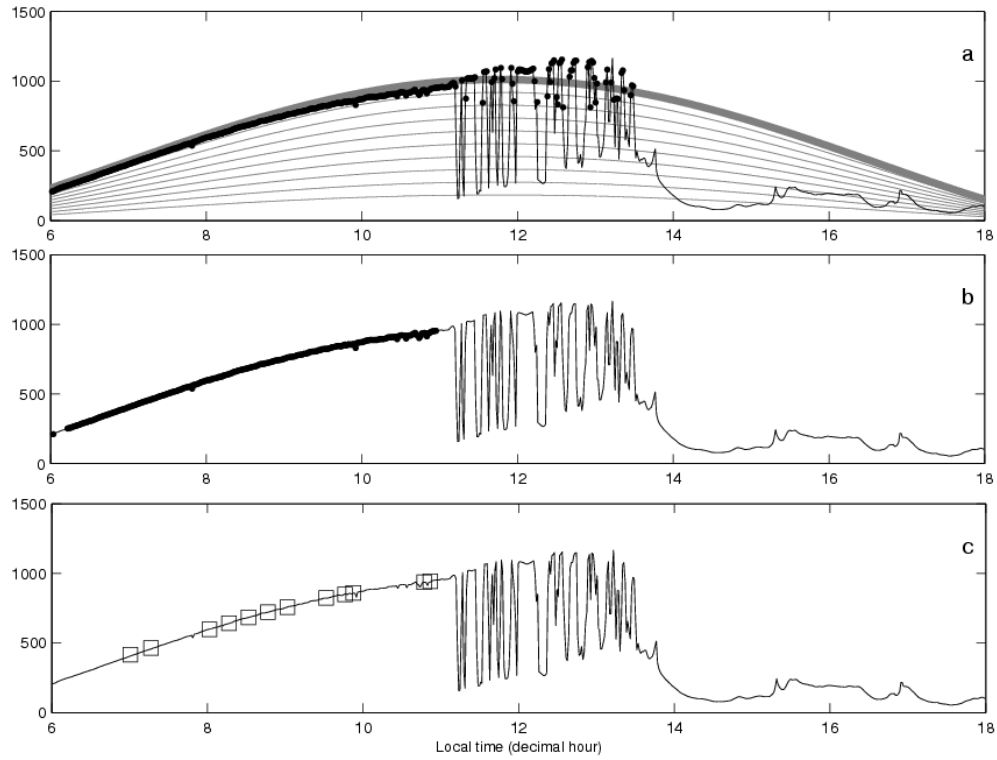


Figure 1. Example plot illustrating how the clear-sky discrimination algorithm works for May 14. The points satisfying clear-sky criteria are highlighted. (a) the first check; (b) the second check; (c) the points with aerosol optical depth are shown as squares.

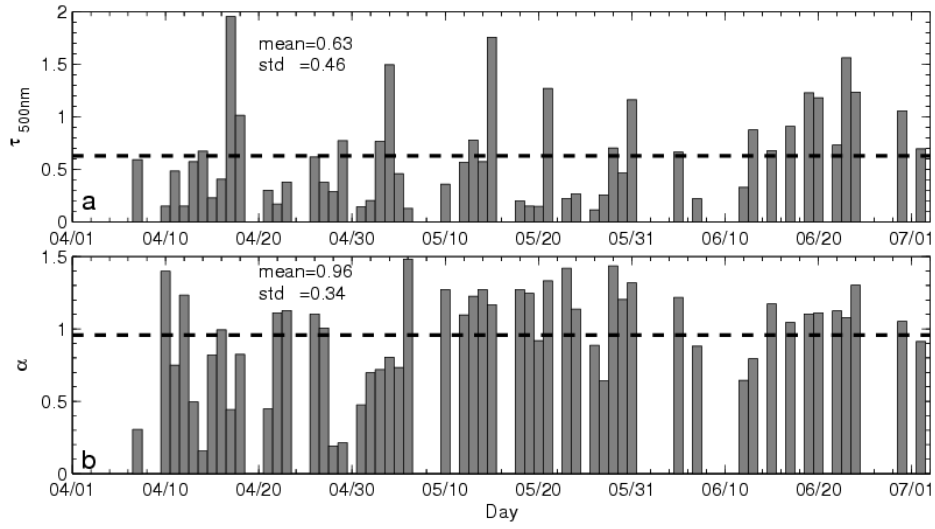


Figure 2. CIMEL Sun/sky radiometer observed time series of daily aerosol optical depth at 500 nm ($\tau_{500\text{nm}}$) (a), and Angstrom wavelength exponent (α) (b) during spring 2005 at Liaozhong. The dashed lines indicate the mean values.

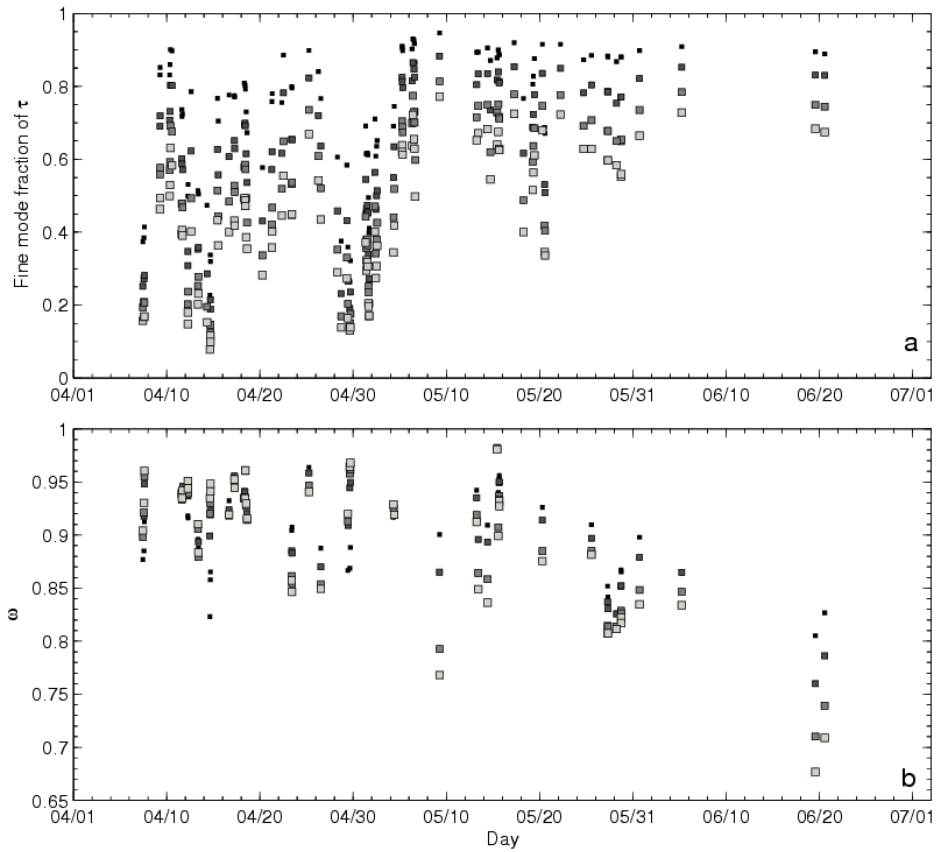


Figure 3. Time series of the contribution of fine mode particles to aerosol optical depth (τ) (a) and time series of the aerosol single scattering albedo (ω) (b). The values at four wavelengths (440, 670, 870, 1020 nm) are depicted by points with sizes varying from small (for 440 nm) to large (1020 nm).

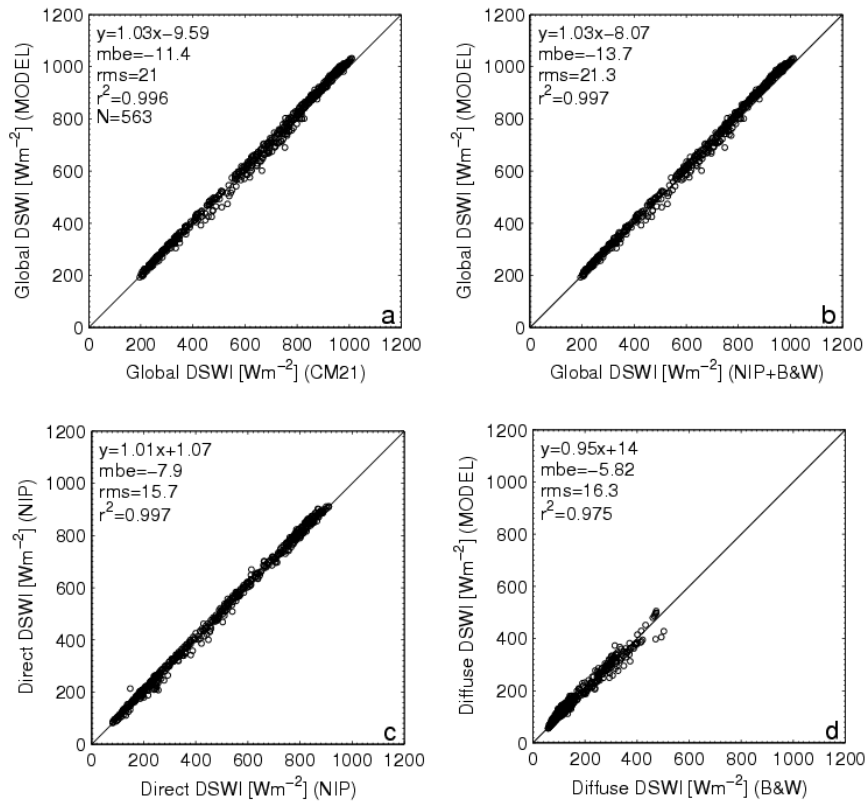


Figure 4. 6S model simulations as a function of (a) global DSWI measured by the CM21 pyranometer (, (b) the sum of direct (NIP) and diffuse (B&W) DSWI, (c) NIP-observed direct DSWI and (d) B&W-observed diffuse DSWI.

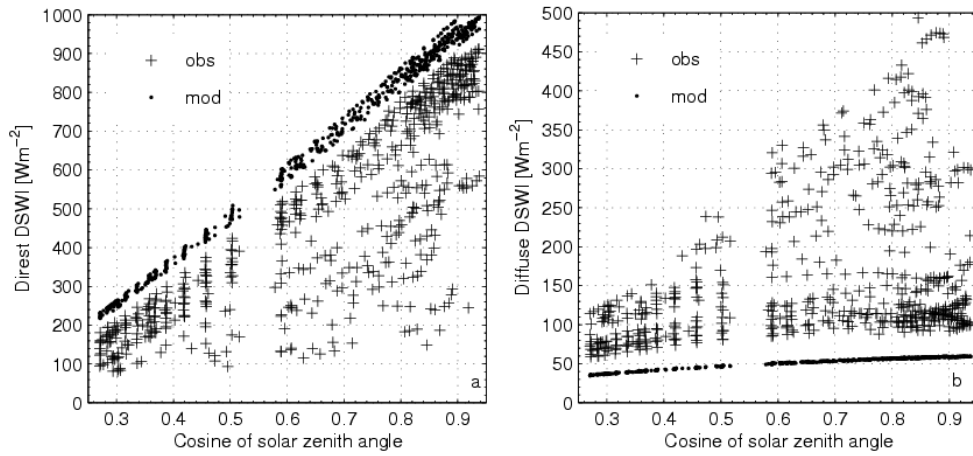


Figure 5. The downward shortwave direct (a) and diffuse (b) irradiances observed by NIP and B&W radiometers and the corresponding modeled background-level irradiances. The observations and simulations are indicated by plus symbols and circles, respectively.

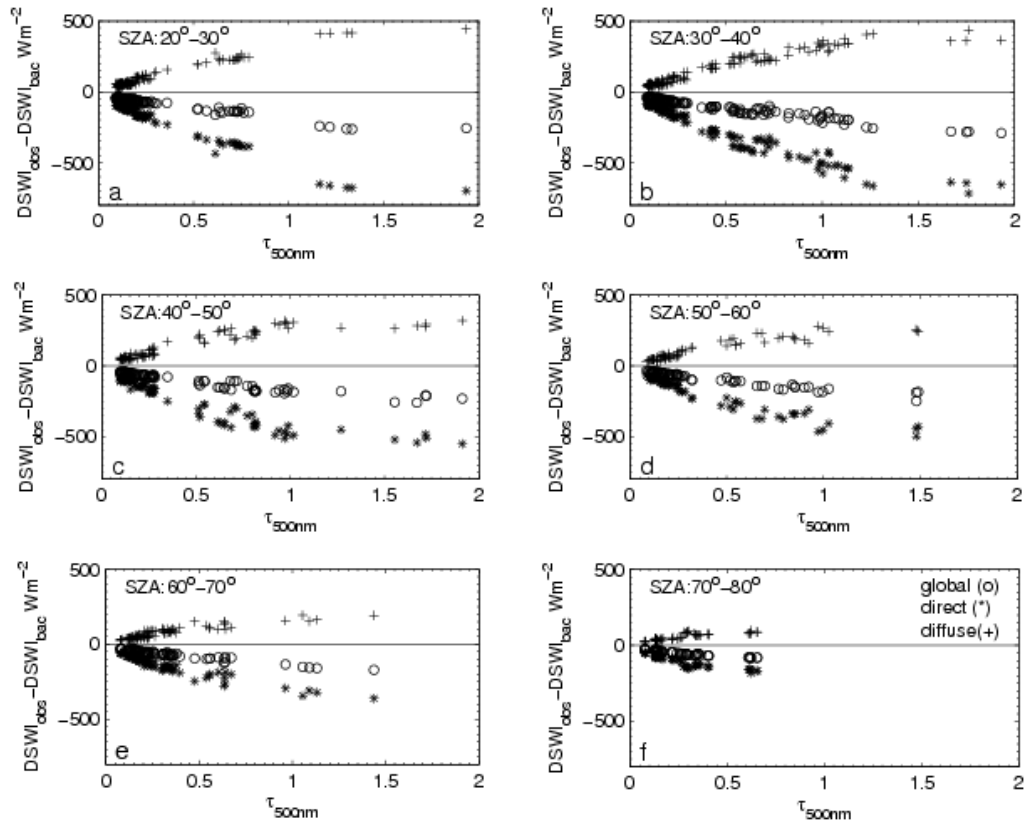


Figure 6. The differences between measured downward shortwave irradiances (DSWI) and corresponding 6S simulations for the background conditions as a function of aerosol optical depth at 500 nm ($\tau_{500\text{nm}}$) in 6 solar zenith angle ranges: 20°-30°; 30°-40°; 40°-50°; 50°-60°; 70°-80°. The global, direct and diffuse DSWI are represented by circle, asterisk and plus symbols, respectively

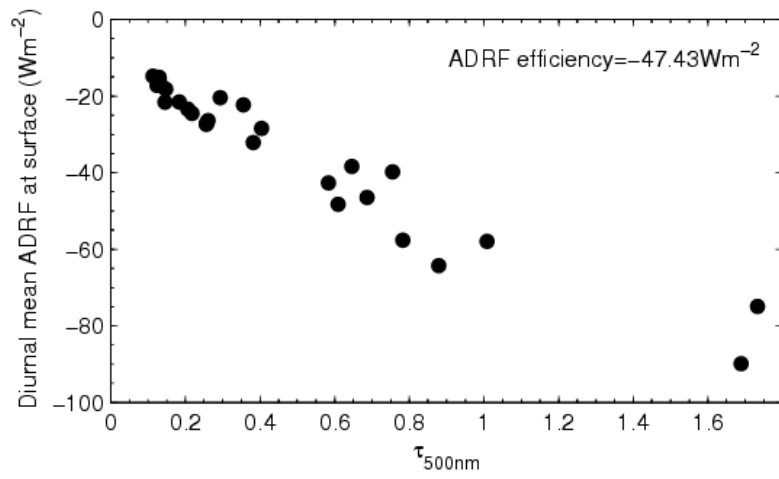


Figure 7. The diurnal aerosol direct radiative forcing (ADRF) at the surface as a function of aerosol optical depth at 500 nm ($\tau_{500\text{nm}}$). The ADRF efficiency is computed from data points with $\tau_{500\text{nm}}$ less than 0.5.